J. Fluid Mech. (1982), *vol.* 123, *pp.* 503–522
Printed in Great Britain

Numerical solution for fully developed flow in heated curved tubes

By J. PRUSA
Department of Mechanical and Industrial Engineering, University of Illinois at Urbana–Champaign, Urbana, IL 61801

AND L. S. YAO
Department of Mechanical and Energy Systems Engineering, Arizona State University, Tempe, AZ 85287

(Received 11 May 1981 and in revised form 30 March 1982)

Fully developed laminar flow for a horizontal heated curved tube is studied numerically. The tube is heated so as to maintain a constant axial temperature gradient. A physical model is introduced that accounts for the combined effects of both buoyancy and centrifugal force. Results, for a Prandtl number of one, are presented for a moderate range of Dean numbers and the product of the Reynolds and Rayleigh numbers. Detailed predictions of the flow resistance, the average heat-transfer rate and the secondary-flow streamlines are given. Also presented are results on the position of the local maxima of shear stress and heat-transfer rate. The numerical results reveal that the mass-flow rate is drastically reduced owing to the secondary flow for a given axial pressure gradient. Consequently, the total heat-transfer rate decreases for a more-curved tube as well as for a larger axial temperature gradient. A flow-regime map is provided to indicate the three basic regimes where (i) centrifugal force dominates, (ii) both buoyancy and centrifugal forces are important, and (iii) buoyancy force dominates.

1. Introduction

Curved tubes and tube bends are extensively employed in many heat-transfer devices such as coiled heat exchangers and various heat engines. They are also often used to cool electronic equipment subject to heating during operation. Engineering design of these devices requires knowledge of the heat-transfer rate from these types of flow given an associated pressure gradient.

Curved-tube flow has been extensively studied both theoretically and experimentally for almost a century (Barua 1963; Collins & Dennis 1975; Dean 1928; Ito 1969; McConalogue & Srivastava 1968; Taylor 1929; Van Dyke 1978). One prominent feature of the flow in curved tubes is the secondary flow.

Centrifugal force, proportional to the square of the axial velocity, tends to push fluid in the central region near point C in figure 1 towards the outer bend of the coiled tube. This induces a pressure gradient directed towards the inner bend of the coiled tube. The induced pressure gradient is almost uniform throughout the cross-section of the tube. The axial velocity, however, varies widely throughout the cross-section. As a result, the centrifugal force acting on the flow varies throughout the cross-section. In the central region, the centrifugal force assumes its greatest magnitude and is roughly in balance with the pressure gradient. The net effect is a smooth movement of fluid axially down the tube. Near the tube wall, the axial velocity is slowed by viscous forces. Here the pressure gradient is stronger than the centrifugal force and forces fluid inward along the top and the bottom of the tube wall. This inward movement along the walls begins at the outer bend, $\psi = 90°$, where fluid from the core first encounters the wall. It ends at the inner bend, $\psi = 270°$, where the two streams meet and then separate from the wall. They then move into the central region and repeat the cycle of motion. The net effect is to produce two vortices of equal magnitude but of opposite sign, with a horizontal line of symmetry separating them.

Another feature of curved-tube flow is a direct consequence of the secondary flow. The secondary flow circulates the high-kinetic-energy fluid from the central core of the tube toward the wall region, where the fluid flows slower. The mixing which results delays the flow transitions. Taylor (1929) found that laminar flow can easily be maintained up to a Reynolds number (based on radius and mean velocity) of 3000, which is three times larger than the critical Reynolds number for the corresponding straight tube.

The parameter characterizing curved-tube flow is the ratio of centrifugal forces to viscous forces and is known as the Dean number $De = \alpha Re^2$. $\alpha = a/R$ denotes the curvature ratio and Re is the Reynolds number. Dean's perturbation analysis, which was the first work to predict theoretically secondary flow in curved tubes, is limited to small De. Numerical methods (Collins & Dennis 1975; McConalogue & Srivastava 1968) have been applied to obtain the solution for the flow of intermediate Dean numbers. The most careful and comprehensive calculations of the flow for $De > 1$ are those of Collins & Dennis (1975). Their results seem to suggest that as $De \rightarrow \infty$, the flow consists of an inviscid core combined with a boundary layer near the tube wall of thickness $O(De^{-\frac{1}{2}})$. The interaction between the core and boundary layer controls the flow field. Their observations support the early approximate theories based on this idea by Barua (1963) and Ito (1969). In particular, the agreement of the flow coefficients from the approximate theories, the numerical solutions, and experimental measurements appear satisfactory. Objections are raised by Van Dyke (1978), however, who considers the importance of the three-dimensional separation near the inner bend. This separation is observed experimentally when $De \gg 1$, and yet has never been modelled in the approximate theory or reproduced by the numerical solutions. The problem is still unclear and the solution remains to be found.†

The effects of secondary flow on heat transfer have also been a favourite subject for the heat-transfer community. Intuitively, one can picture that the local heat-transfer rate increases near the outer bend, where the local flow is similar to a stagnation-point flow. Near the inner bend, the heat-transfer rate is a local minimum owing to the reversed stagnation-point flow. A perturbation solution by Ozisik & Topakoglu (1968) provides information on the variation of heat-transfer rate as a function of De and Prandtl number Pr. Their analysis is limited to small De and α; yet their predictions agree well with the experiments of Seban & McLaughlin (1963) and Mori & Nakayama (1965). Numerical studies by Akiyama & Cheng (1971), and Kalb & Seader (1972), among others (Patankar, Pratap & Spalding 1974; Rabadi, Chow & Simon 1979; Simon, Chang & Chow 1977; Yee & Humprey 1979; Zapryanov, Christov & Toshov 1980), provides correlations for the effects of De and Pr on heat-transfer rates for intermediate Dean numbers. A common finding is that the

---

† Dennis (1980) has recently suggested that the discrepancy between Van Dyke's series solution and all previous solutions may be due to 'flow bifurcation'. This non-uniqueness of solutions may characterize curved-tube flow for large De.

secondary flow enhances heat-transfer rates. A common assumption throughout these studies is that the momentum and energy equations are uncoupled.

Morton (1959) showed, however, for the case of a straight tube, that a secondary flow composed of two vertical vortices is generated by the buoyancy force. The heat-transfer rate is enhanced by the secondary flow, and is larger than would be expected without the buoyancy effect given the same mass-flow rate. Morton found that the buoyancy force is proportional to the product *ReRa* of Reynolds and Rayleigh numbers. Since his analysis is a perturbation method, it is limited to small values of the product *ReRa*. A similar perturbation analysis for curved-tube flow (Yao & Berger 1978) shows that the buoyancy effect can indeed be as important as the effect produced by centrifugal force. For a horizontally positioned coiled tube, the dividing streamline between two vortices is neither horizontal or vertical. It is the result of two perpendicular forces. Consequently, the local maximum and minimum heat transfer rates do not necessary occur at the outer and inner bends. Since the perturbation solution is valid only for small *De* and *ReRa* it does not provide information about the extra pumping power required to maintain the mass-flow rate or give the variation of total heat-transfer rate, as a function of the buoyancy modified secondary flow.

The present paper is motivated by interest in demonstrating the effects of buoyancy as well as centrifugal force. A numerical method is applied to study the flow field and the temperature distribution in a hydrodynamically and thermally fully developed flow in a horizontally positioned coiled tube. The numerical solution is valid for intermediate ranges of *De* and *ReRa*. The numerical results clearly demonstrate that the mass flow rate is drastically reduced owing to the secondary flow under a given axial pressure gradient. The total heat-transfer rate decreases for a more-curved tube as well as for a larger overheating condition, i.e. a larger axial temperature gradient. This is a consequence of the reduction of the mass-flow rate. The numerical results provide a flow-regime map to indicate the three basic regimes where (i) centrifugal force dominates, (ii) both buoyancy and centrifugal forces are important, and (iii) buoyancy force dominates.

2. Analysis

A truly general solution to the problem of heat transfer in curved tubes is, at present, an intractable problem. In order to make meaningful progress one must simplify the general equations governing the flow as much as possible, using physical insight to bring out only the most important terms of the general equations. In this respect, this paper departs from all previous numerical work because it includes a buoyancy term in the momentum equations.

The physical model considered is one with constant axial pressure and temperature gradients, with the fluid flowing into the direction of increasing temperature. Such conditions are encountered in flow through metal tubes (good thermal conductivity) with a constant-heat-flux boundary condition.

We begin with the basic equations for laminar flow set out in the perturbation analysis (Yao & Berger 1978):

$$\frac{1}{\bar{r}}\frac{\partial(\overline{ru})}{\partial\bar{r}}+\frac{1}{\bar{r}}\frac{\partial\bar{v}}{\partial\psi}+\frac{\bar{u}\sin\psi+\bar{v}\cos\psi}{R+\bar{r}\sin\bar{\psi}}=0, \tag{1a}$$

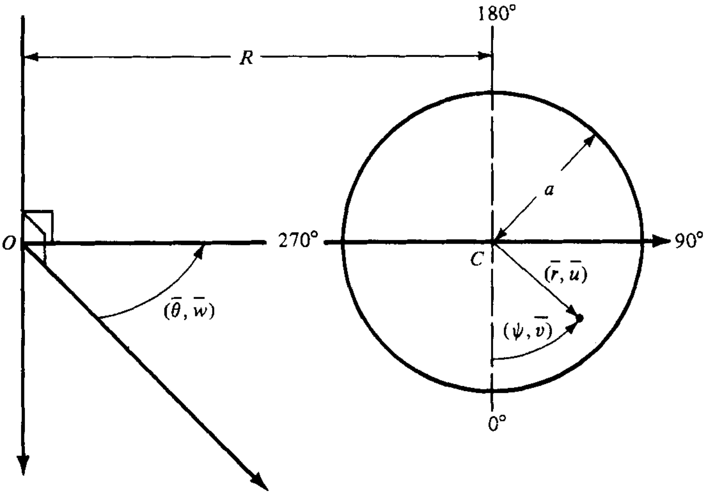

FIGURE 1. Co-ordinate system.

$$\bar{u}\frac{\partial \bar{u}}{\partial \bar{r}}+\frac{\bar{v}}{\bar{r}}\frac{\partial \bar{u}}{\partial \psi}-\frac{\bar{v}^2}{\bar{r}}-\frac{\bar{w}^2 \sin\psi}{R+\bar{r}\sin\psi}-\beta g(T_{\mathrm{w}}-\bar{T})\cos\psi$$
$$=\frac{-1}{\rho}\frac{\partial \bar{p}}{\partial \bar{r}}-\nu\left(\frac{1}{\bar{r}}\frac{\partial}{\partial\psi}+\frac{\cos\psi}{R+\bar{r}\sin\psi}\right)\left(\frac{\partial \bar{v}}{\partial \bar{r}}+\frac{\bar{v}}{\bar{r}}-\frac{1}{\bar{r}}\frac{\partial \bar{u}}{\partial \psi}\right), \tag{1b}$$

$$\bar{u}\frac{\partial \bar{v}}{\partial \bar{r}}+\frac{\bar{v}}{\bar{r}}\frac{\partial \bar{v}}{\partial \psi}+\frac{\overline{uv}}{\bar{r}}-\frac{\bar{w}^2 \cos\psi}{R+\bar{r}\sin\psi}+\beta g(T_{\mathrm{w}}-\bar{T})\sin\psi$$
$$=\frac{-1}{\rho\bar{r}}\frac{\partial \bar{p}}{\partial \psi}+\nu\left(\frac{\partial}{\partial\bar{r}}+\frac{\sin\psi}{R+\bar{r}\sin\psi}\right)\left(\frac{\partial \bar{v}}{\partial \bar{r}}+\frac{\bar{v}}{\bar{r}}-\frac{1}{\bar{r}}\frac{\partial \bar{u}}{\partial \psi}\right), \tag{1c}$$

$$\bar{u}\frac{\partial \bar{w}}{\partial \bar{r}}+\frac{\bar{v}}{\bar{r}}\frac{\partial \bar{w}}{\partial \psi}+\frac{\bar{w}(\bar{u}\sin\psi+\bar{v}\cos\psi)}{R+\bar{r}\sin\psi}$$
$$=\frac{-1}{\rho(R+\bar{r}\sin\psi)}\frac{\partial \bar{p}}{\partial \bar{\theta}}+\nu\left[\left(\frac{\partial}{\partial\bar{r}}+\frac{1}{\bar{r}}\right)\left(\frac{\partial \bar{w}}{\partial \bar{r}}+\frac{\bar{w}\sin\psi}{R+\bar{r}\sin\psi}\right)\right.$$
$$\left.+\frac{1}{\bar{r}}\frac{\partial}{\partial\psi}\left(\frac{1}{\bar{r}}\frac{\partial \bar{w}}{\partial \psi}+\frac{\bar{w}\cos\psi}{R+\bar{r}\sin\psi}\right)\right], \tag{1d}$$

$$\bar{u}\frac{\partial \bar{T}}{\partial \bar{r}}+\frac{\bar{v}}{\bar{r}}\frac{\partial \bar{T}}{\partial \psi}+\frac{\bar{w}}{R+\bar{r}\sin\psi}\frac{\partial \bar{T}}{\partial \bar{\theta}}$$
$$=\frac{\sigma}{\bar{r}(R+\bar{r}\sin\psi)}\left\{\frac{\partial}{\partial\bar{r}}\left[\bar{r}(R+\bar{r}\sin\psi)\frac{\partial \bar{T}}{\partial \bar{r}}\right]\right.$$
$$\left.+\frac{\partial}{\partial\psi}\left[(R+\bar{r}\sin\psi)\frac{1}{\bar{r}}\frac{\partial \bar{T}}{\partial \psi}\right]+\frac{\partial}{\partial\bar{\theta}}\left[\frac{\bar{r}}{R+\bar{r}\sin\psi}\frac{\partial \bar{T}}{\partial \bar{\theta}}\right]\right\}. \tag{1e}$$

where ρ is the density, ν is the kinematic viscosity, σ is the thermal diffusivity, β is the coefficient of expansion, and g is the acceleration due to gravity. Note that the buoyancy forces are approximated by the Boussinesque form in these equations. These equations are based on a system of toroidal co-ordinates as shown in figure 1. The radius of the circle in which the tube is coiled is denoted by R and that of the tube by a. $R\bar{\theta}$ measures the axial distance from a given plane of reference.

In order to simplify (1*a–e*), we assume fully developed flow. This implies that $\partial\xi/\partial\bar{\theta} = 0$ for $\xi = \bar{u}$, $\bar{n}$ and $\bar{w}$.

Our choice of velocity scale is based upon the given pressure gradient, G. For flow through an unheated straight tube, the maximum or centreline velocity is $Ga^2/4\mu$. This provides a natural velocity scale for the problem; it allows immediate, absolute comparisons in flow velocity and volume rates of flow for a heated curved tube with those of an unheated straight tube for a given radius and pressure gradient.

Denoting the temperature gradient along the tube by τ, the wall temperature by T_{w} and the reference wall temperature by T_0, we define the following set of dimensionless variables:

$$\left.\begin{aligned}
&r = \bar{r}/a, \quad \theta = R\bar{\theta}/aRe \quad \text{(co-ordinates)},\\
&w = \frac{\bar{w}}{Ga^2/4\mu}, \quad u = \frac{\bar{u}}{\nu/a}, \quad v = \frac{\bar{v}}{\nu a}. \quad \text{(velocities)},\\
&T = \frac{T_{\mathrm{w}} - \bar{T}}{\tau a Pe}, \quad T_{\mathrm{w}} = T_0 + \tau R\bar{\theta} \quad \text{(temperature)},\\
&p = \frac{\bar{p}}{\rho G^2 a^4/16\mu^2} \quad \text{(pressure)},\\
&\alpha = \frac{a}{R}, \quad De = \alpha Re^2 \quad \text{(Dean number)},\\
&Pr = \frac{\nu}{\sigma} \quad \text{(Prandtl number)}, \quad Re = \frac{Ga^3}{4\mu\nu} \quad \text{(Reynolds number)},\\
&Pe = \frac{Ga^3}{4\mu\sigma} \quad \text{(Peclet number)}, \quad Ra = \frac{\beta g a^4 \tau}{\nu\sigma} \quad \text{(Rayleigh number)}.
\end{aligned}\right\} \tag{2}$$

This is essentially the non-dimensionalization used in Yao & Berger (1978); the differences are in the choice of temperature scale and definition of Dean number.

Equations (2) are substituted into (1) and terms $O(\alpha)$ or smaller are dropped. The pressure terms of (1*b*, *c*) are then eliminated by cross-differentiation. Finally, a dimensionless stream function f defined by

$$u = -r^{-1}\frac{\partial f}{\partial\psi}, \quad v = \frac{\partial f}{\partial r} \tag{3}$$

is introduced to satisfy continuity identically. The following system of four simultaneous partial differential equations then results:

$$\nabla^2 w - \frac{\partial p}{\partial\theta} = \frac{1}{r}\frac{\partial(f, w)}{\partial(r, \psi)}, \tag{4a}$$

$$\nabla^2 T + w = \frac{Pr}{r}\frac{\partial(f, T)}{\partial(r, \psi)}, \tag{4b}$$

$$\nabla^2 f = -\Omega, \tag{4c}$$

$$\nabla^2\Omega - \frac{1}{r}\frac{\partial(f, \Omega)}{\partial(r, \psi)} = De\left[\frac{\partial w^2}{\partial r}\cos\psi - \frac{1}{r}\frac{\partial w^2}{\partial\psi}\sin\psi\right] - ReRa\left[\frac{\partial T}{\partial r}\sin\psi + \frac{1}{r}\frac{\partial T}{\partial\psi}\cos\psi\right], \tag{4d}$$

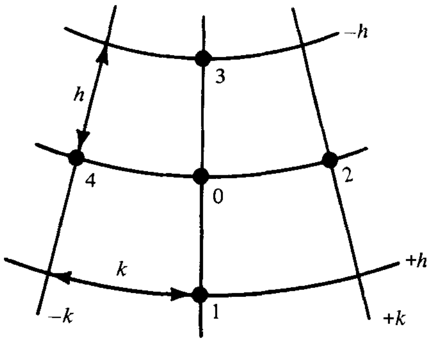

FIGURE 2. Computation mesh.

where Ω is the dimensionless vorticity and

$$\nabla^2 = \frac{\partial^2}{\partial r^2}+\frac{1}{r}\frac{\partial}{\partial r}+\frac{1}{r^2}\frac{\partial^2}{\partial \psi^2}, \quad \frac{\partial(\xi,\eta)}{\partial(r,\psi)} = \frac{\partial \xi}{\partial r}\frac{\partial \eta}{\partial \psi}-\frac{\partial \xi}{\partial \psi}\frac{\partial \eta}{\partial r}, \quad \frac{\partial p}{\partial \theta} = -4.$$

Note that the last expression results from both the non-dimensionalization given in (2) and from the assumption that the axial pressure gradient is constant. One must keep in mind the constraints imposed by the development of the governing equations (4), on *Re* and α; that is, *Re* must be small enough to maintain laminar flow and $O(\alpha) \ll 1$. The first term on the right-hand side of (4*d*) represents centrifugal force and will cause the particles in the fluid core to move towards the outside bend of the tube. The second term is due to the buoyancy effect and will cause the cooler fluid in the core to fall. The combined effect generates two vortices whose line of symmetry lies at an angle with respect to either the horizontal or vertical directions. Note that this line of symmetry is curved. Note also that the strength of the buoyancy effect is proportional to *ReRa* (Morton 1959). This means that the buoyancy effect is proportional to both the axial temperature gradient and to the characteristic axial velocity. The boundary conditions for the system (4) are

$$\left.\begin{aligned} w = f = T = 0, \quad \Omega = -\frac{\partial^2 f}{\partial r^2} \quad (r = 1),\\ \Omega = f = 0 \quad (r = 0). \end{aligned}\right\} \tag{5}$$

Computational boundary conditions for w and T at $r = 0$ are developed in §3.

3. Numerical method

In order to obtain an approximate solution to the system (4) of simultaneous equations, we must transform them into a system of finite-difference equations appropriate for computation on a high-speed computer. We divide the circular cross-section of the tube (figure 1) into a grid formed by a set of radial lines that cut a set of circular arcs concentric with the boundary $r = 1$. The nodes are uniformly spaced with increment h in the radial direction r, and k in the angular direction ψ. Southwell's (1946) notation is used for the immediate neighbourhood of a typical node (figure 2).

The method of approximating equations (4*a*, *b*, *d*) with finite-difference equations follows that used in Collins & Dennis (1975). Defining the parameters

$$2\Gamma = \frac{1}{r}\left(1+\frac{\partial f}{\partial \psi}\right), \quad 2\Delta = \frac{1}{r}\frac{\partial f}{\partial r}, \tag{6a}$$

it can be shown that the momentum equation leads to the result

$$w_0 = \frac{(A+B+C)h^2}{2+2|\Gamma|h+h^2(2/r_0^2+2|\Delta|k)/k^2}, \tag{6b}$$

where

$$A = \tfrac{1}{2}\{w_1[1+[\Gamma+|\Gamma|)\,h]+w_3[1-(\Gamma-|\Gamma|)]\,h\} + \frac{1}{k^2}\left\{w_2\left[\frac{1}{r_0^2}-(\Delta-|\Delta|)\,k\right]+w_4\left[\frac{1}{r_0^2}+(\Delta+|\Delta|)\,k\right]\right\}, \tag{6c}$$

$$B = -\left[\frac{|\Gamma|}{h}\,(w_1+w_3-2w_0)+\frac{|\Delta|}{k}\,(w_2+w_4-2w_0)\right], \tag{6d}$$

$$C = 4. \tag{6e}$$

Note that while (6*b*) is completely equivalent to a second-order central-differencing method, a doner-cell (second-upwind-differencing) method results if the *B*-term is ignored. In a similar fashion, the vorticity equation (4*d*) leads to equations identical in form with (6*b*–*d*), with w_0, w_1, w_2, w_3 and w_4 replaced by Ω_0, Ω_1, Ω_2, Ω_3, Ω_4 and

$$C = De\left[\frac{w_0(w_2-w_4)\sin\psi_0}{r_0h}\,\frac{-w_0(w_1-w_3)\cos\psi_0}{h}\right] + ReRa\left[\frac{(T_2-T_4)\cos\psi_0}{2r_0k}+\frac{(T_1-T_3)\sin\psi_0}{2h}\right]. \tag{6f}$$

Differencing of (4*b*) requires a slight modification of (6*a*). We define

$$2\bar{\Gamma} = \frac{1}{r}\left[1+Pr\frac{\partial f}{\partial \psi}\right], \quad 2\bar{\Delta} = \frac{Pr}{r}\frac{\partial f}{\partial r}. \tag{6g}$$

With these slightly modified parameters, the energy equation leads to the system of relations (6*b*–*d*), with w_i, Γ, Δ replaced by

$$T_i,\ \bar{\Gamma},\ \bar{\Delta} \quad \text{for} \quad i = 0, \ldots, 4 \quad \text{and} \quad C = w_0. \tag{6h}$$

Central differencing is used on the stream function (4*c*). The result, using Gauss–Seidel iteration, is

$$f_0^{m+1} = \frac{D}{E}, \tag{7a}$$

where

$$D = \Omega_0^{m+1}\,h^2+\left(1+\frac{h}{2r_0}\right)f_1^m+\left(1-\frac{h}{2r_0}\right)f_3^{m+1}+\frac{h^2}{r_0^2\,k^2}\,(f_2^m+f_4^{m+1}), \tag{7b}$$

$$E = \frac{2(1+h^2)}{r_0^2\,k^2}f_0^m. \tag{7c}$$

Vorticity at the boundary $r = 1$ is approximated by the finite-difference form

$$\Omega_N = \frac{-2f_{N-1}}{h^2}, \tag{8}$$

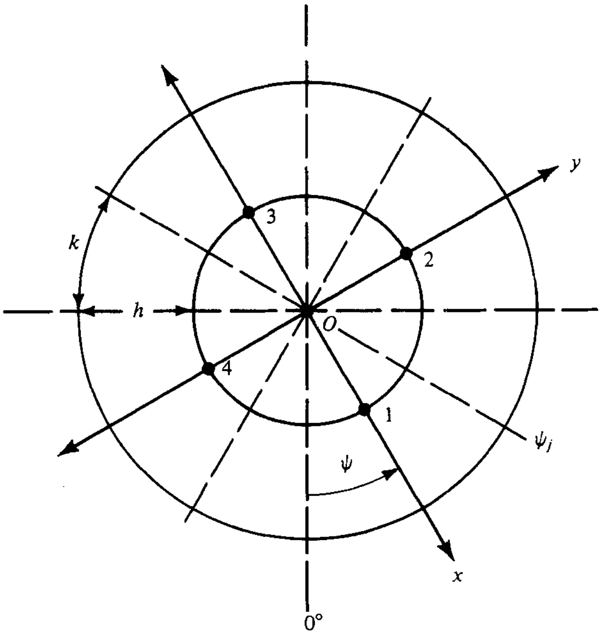

FIGURE 3. Local neighbourhood of the central mode.

where the subscript N denotes a node position on the boundary $r = 1$. This formula is the result of central differencing coupled with a no-slip condition (imposed by $v_N = 0$).

Although the remaining boundary conditions given in (5) are straightforward, one needs to describe boundary conditions for w and T at $r = 0$. Since the centre point $r = 0$ is multiply defined in toroidal co-ordinates, natural computational boundary conditions are that the values of w and T at $r = 0$ be uniquely defined. In order to ensure this, we transform the immediate neighbourhood of the central node into Cartesian co-ordinates.

Transformations of the momentum and energy equations (4a, b), into Cartesian forms appropriate for this neighbourhood of the central node are

$$\frac{\partial^2 w}{\partial x^2}+\frac{\partial^2 w}{\partial y^2}+4 = -\frac{\partial f}{\partial y}\frac{\partial w}{\partial x}+\frac{\partial f}{\partial x}\frac{\partial w}{\partial y}, \tag{9a}$$

$$\frac{\partial^2 T}{\partial x^2}+\frac{\partial^2 T}{\partial y^2}+w = Pr\left(\frac{\partial f}{\partial x}\frac{\partial T}{\partial y}-\frac{\partial f}{\partial y}\frac{\partial T}{\partial x}\right), \tag{9b}$$

where x and y are the Cartesian axes through the central node. Using centred differencing, we obtain from (9)

$$w_0 = \tfrac{1}{4}(w_1+w_2+w_3+w_4)+h^2+\tfrac{1}{16}[(f_2-f_4)(w_1-w_3)-(f_1-f_3)(w_2-w_4)], \tag{10a}$$

$$T_0 = \tfrac{1}{4}(T_1+T_2+T_3+T_4+h^2 w_0)+\tfrac{1}{16}Pr[(f_2-f_4)(T_1-T_3)-(f_1-f_3)(T_2-T_4)]. \tag{10b}$$

Equations (10a, b) are solved for each orientation of the Cartesian axes corresponding to a distinct value of ψ (figure 3). The multiple co-ordinates of the central node have been found to give a unique value of w and T using this method.

Equations (6)–(8), and (10) are now sufficient to obtain numerical approximations to w, T, Ω and f for given values of Pr, De, and $ReRa$.

4. Computational procedure

The strategy in solving the preceding system of equations is twofold. First, in an effort to make the iterative method more stable, a solution to the system (4) is calculated with the B-terms (6*d*) set equal to zero. Once this solution has been obtained, it is used as the initial condition for the more-accurate method, which includes the B-terms. This essentially is the difference-correction procedure of Fox (1947) as given in Collins & Dennis (1975). It has both the advantages of the stability of an upwind-differencing method and the accuracy of a central-difference method. The first solution is also called the uncorrected solution since it is only first-order accurate, while the more accurate solution is called the corrected solution.

A Gauss–Seidel iteration method is used for the momentum, energy and vorticity equations as well as for the stream-function equation. At every stage of the computation, only the most recent values of the dependent variables are used. The iteration sequence is executed in the following order.

(i) The central node values for w and T are calculated according to (10).

(ii) The momentum equation is solved according to (6) using the new values for $w(r = 0)$, old values of f or w, and new values of w as they become available.

(iii) The energy equation is solved using the new values of w and $T(r = 0)$, old values of f or T, and new values of T as they become available.

(iv) The vorticity equation is solved using the new values of w and T, old values of f or Ω, and new values of Ω as they become available.

(v) The stream-function equation is solved according to (7).

This sequence is repeated until the solution converges to within a prescribed criterion of precision. Since vorticity appears to be the most sensitive variable, we use it to define the convergence criterion. If, between two successive iterations,

$$|\Omega^{m+1}-\Omega^{m}| < 5\times 10^{-5} \qquad (11)$$

throughout the computational domain, then we consider the solution to have converged.

Under-relaxation of the iterations has been found to be necessary in order to obtain convergence of the solution. Two relaxation parameters ω_1 and ω_2 have been introduced into the iterations. The second relaxation parameter ω_2 is applied only to the second-order central-differencing method. It is used in the momentum calculation in the following way:

$$(A+B+C)^{m+1} = (A+C)^{m+1}+\omega_2\, B^{m+1}+(1-\omega_2)\, B^{m}, \qquad (12a)$$

where A, B and C are defined in (6). Note that A, B and C use the most recent values of w. For example B^m uses the m iteration values for w_3 and w_4, and the $m-1$ iteration values for w_0, w_1, and w_2. This relaxation formulation is also used in the energy and vorticity calculations. The first relaxation parameter ω_1 is used only in the vorticity calculation at the surface of the tube according to

$$\Omega_N^{m+1} = \omega_1(-2f_{N-1}^{m}/h^2)+(1-\omega_1)\,\Omega_N^{m}. \qquad (12b)$$

The stream-function calculation is not under-relaxed. The values $\omega_1 = 0{\cdot}25$ and $\omega_2 = 0{\cdot}05$ have been found to be suitable for our range of calculations.

In order to help ensure that the computations converge quickly, one must carefully consider the choice of initial conditions. For cases of low *De* and *ReRa*, we have used the velocity and temperature profiles of Poiseuille flow in a straight tube with a constant axial temperature gradient. These cases would provide initial conditions for computations with more moderate values of *De* and *ReRa*, which would then be used to start computations with even higher values of the two dimensionless parameters. Generally we would keep either *De* or *ReRa* constant and monotonically increase the other parameter in order to demonstrate clearly the effect of variation of one parameter against the other. The range of our computations covers the values $0 \leqslant De \leqslant 31250$ and $0 \leqslant ReRa \leqslant 20000$. For heated straight-tube flow ($De = 0$), *ReRa* was extended up to 50000. In all cases, we set $Pr = 1$.

Since the dividing streamline between the two vortices is generally not a straight line, symmetry along the dividing streamline cannot be used as a boundary condition. As a result, our computational mesh covers the entire cross-section of the tube. In order to keep computation times moderate, we have chosen the values $h = 0{\cdot}05$ and $k = \frac{1}{24}\pi$ for our mesh. With this grid size, 200 to 400 s on a CDC 175 are required to obtain converged solutions.

The accuracy of our corrected solutions may be judged from the results of Collins & Dennis (1975), since our computational methods are essentially the same. A direct comparison is readily made using the lowest friction-ratio curve of figure 4, which corresponds to $ReRa = 0$. This curve can be seen to lie very close – within 0·8 % – to the results of Collins & Dennis. It appears that for the case $ReRa = 0$, our results essentially duplicate those of Collins & Dennis, and thus are unlikely to be in error by more than 1 or 2 %. Although direct comparisons for the non-zero values of *ReRa* are not possible, some evidence of the accuracy of these solutions is given by comparison of the uncorrected and corrected solutions. It is found that the uncorrected solutions for larger values of *ReRa* differ from the corrected solutions by less than 6 %. Since the corrected solutions are considerably more accurate than the uncorrected solutions, we conclude that in all cases our corrected solutions should be in error by, at the very most, 5 %, and likely are in error by no more than 1 or 2 %.

All results described in §5 are based on the central-difference corrected solution.

5. Results and discussion

The effects of buoyancy on the flow and heat transfer through curved tubes manifest themselves in several ways. Most obvious are variations in the values of global parameters such as in the friction coefficient γ or total heat flux Q. Less observable, though often pronounced, are variations at a local level, such as positions of maximum heat transfer or shear stress.

5.1 *Ratio of coefficients of friction*

Results of the present analysis are best compared with previous work by examining the calculated values of γ_c/γ_s, which is the ratio of the coefficients of friction for a curved and a straight tube respectively, for varying values of *De* and *ReRa*. In order to match our data precisely with earlier results, we choose to present the data with respect to the modified Dean number as presented in Collins & Dennis (1975):

$$\kappa = 2\alpha^{\frac{1}{2}}\, Re_{\mathrm{m}},$$

where Re_{m} is modified Reynolds number based upon a mean axial velocity (recall that $\alpha = a/R$). Letting the dimensionless volume rate of flow be denoted by *WM*, with

$$WM = \frac{1}{\pi}\int_0^1\int_0^{2\pi} wr\, dr\, d\psi,$$

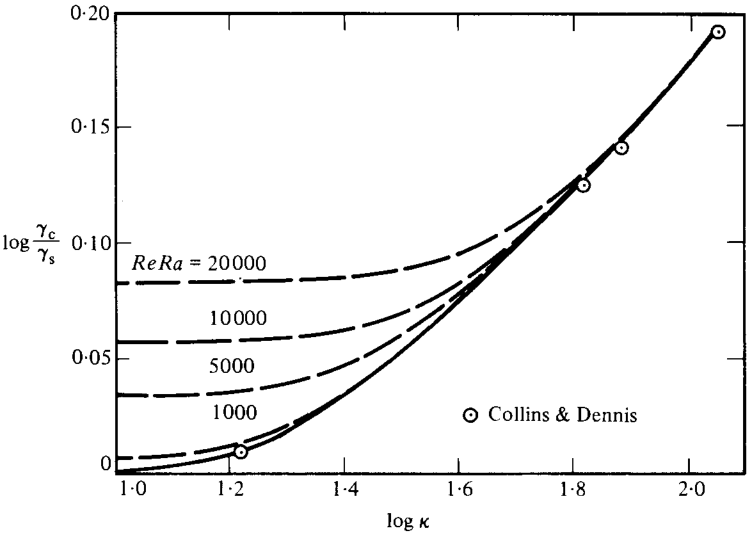

FIGURE 4. Variation of the friction ratio γ_c/γ_s with κ and *ReRa*

which is calculated in the numerical solutions, we find $Re_m = ReWM$. Thus we can calculate κ according to the expression

$$\kappa = 2WMDe^{\frac{1}{2}}. \tag{13}$$

Since $w = 1 - r^2$ is the axial-velocity distribution for straight-tube flow and since it may be shown that $\gamma_c/\gamma_s = WM_s/WM$, where WM_s is the volume rate of flow through a straight tube corresponding to a given pressure gradient G, we obtain

$$\gamma_c/\gamma_s = 0{\cdot}5/WM. \tag{14}$$

The variation of the ratio of friction coefficients with κ and *ReRa* is shown in figure 4. The curves of constant *ReRa* demonstrate a very simple result; that *ReRa* acts like *De* in that the ratio of friction coefficients increases with increasing *ReRa*. This is because of the effect that buoyancy will act to increase the magnitude of the secondary flow beyond that which is expected from centrifugal force alone. More kinetic energy of the flow is directed into the secondary flow, and as a result frictional losses increase. For a given *ReRa*, as *De* increases, the flow becomes ever more dominated by the centrifugal force. Eventually the contribution to the secondary flow by the buoyancy force becomes negligible. For this reason, the curves of constant *ReRa* approach the lowest or base curve for $ReRa = 0$ asymptotically as $De \rightarrow \infty$. From a practical viewpoint it is observed, for a given *ReRa*, that once *De* has increased beyond a certain value the flow is dominated completely by the centrifugal force. In this regime, the influence of buoyancy is unimportant and the momentum and energy equations may safely be considered to be uncoupled.

Note that the effects of buoyancy on the friction coefficient for a straight tube may be calculated simply by setting $De = 0$ for non-zero *ReRa*. Such computations have been carried out and compare favourably with the perturbation analysis developed by Morton (1959). Morton claims that his solution, based on a three-term series, is accurate to within 10 % up to $ReRa = 3000$. Our numerical computations of the ratio

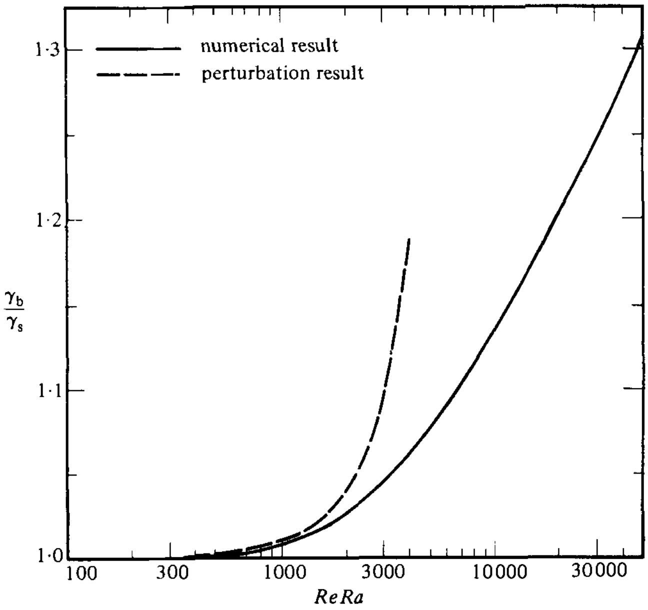

FIGURE 5. Variation of the friction ratio γ_b/γ_s with *ReRa* in straight tubes.

of the coefficients of friction are compared directly with the perturbation result (Morton 1959)

$$\gamma_b/\gamma_s = 1 + 0{\cdot}4202\ (ReRa/4608)^2 + \dots$$

in figure 5. Here γ_b is the friction coefficient for flow through a straight tube with buoyancy, for a given pressure gradient. Morton's result is seen to overpredict γ_b/γ_s compared with our results by

(i) 1 % at $ReRa = 1000$,
(ii) 5 % at $ReRa = 2000$,
(iii) 12 % at $ReRa = 3000$.

For $ReRa > 3000$, the higher-order terms not computed by Morton become very important. Consequently, the perturbation result diverges rapidly from the numerical result. Note that the increase in the ratio of the coefficients of friction with *ReRa*, as explained for figure 4, is clearly demonstrated.

The present numerical results can be observed to extend well beyond the range of validity of the perturbation solution for global shear stress by Yao & Berger (1978), since the perturbation solution predicts $\gamma_c/\gamma_s = 1$.

5.2 *Ratio of average heat-transfer rates*

The second global parameter of interest is the total heat flux Q. Denoting the dimensionless local heat-transfer flux q by

$$q(\psi) = \left(\frac{\partial T}{\partial r}\right)_{r=1}, \tag{15}$$

we define the total or average heat flux Q as

$$Q = \frac{1}{2\pi}\int_0^{2\pi} q(\psi)\, d\psi. \tag{16}$$

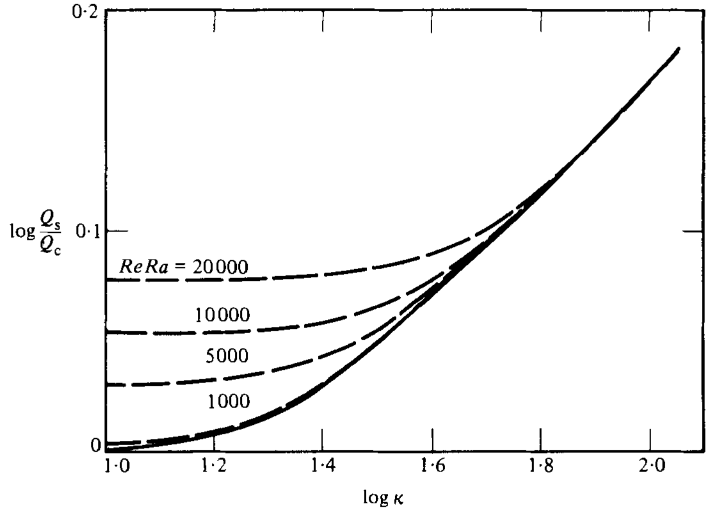

FIGURE 6. Variation of average heat-transfer ratio Q_s/Q_c with κ and *ReRa*.

Both Q and q are calculated in the numerical solutions. Note that the local and average Nusselt number Nu may be computed readily from the dimensionless $q(\psi)$ and Q according to

$$Nu(\psi) = -Pe\, q(\psi), \quad Nu_{\mathrm{av}} = -Pe\, Q. \tag{17}$$

We choose $T = \frac{1}{16}(3-4r^2+r^4)$, as is standard, to be the temperature distribution for straight-tube flow with a constant axial temperature gradient τ. From this, we determine that the ratio of average heat-transfer rates is

$$Q_s/Q_c = 0{\cdot}25/Q, \tag{18}$$

where Q_s and Q_c are the heat-transfer rates for a straight (with no buoyancy and curved tube respectively, for a given pressure gradient G.

The variation of the ratio of average heat fluxes with κ and *ReRa* is shown in figure 6. Note the striking resemblance to figure 4. Again it becomes clear that the effect of *ReRa* is similar to that of *De*. An important difference when compared with the friction coefficient is that the average heat-transfer rate decreases with increasing *ReRa* or increasing *De*. This result apparently contradicts many earlier works. We observe that the average heat-transfer rate decreases because the volume rate of flow decreases for increasing *ReRa* or *De* for a given pressure gradient. The volume rate of flow must decrease because the friction coefficients increase as shown in figure 4. Again, we conclude that the magnitude of the secondary flow increases with *ReRa*. One further observation from figure 6 is that the curves of constant *ReRa* approach asymptotically the lowest or base curve corresponding to *ReRa* = 0. The reasoning for this behaviour is precisely the same as given for the friction-coefficient curves of figure 4. As *De* increases, the centrifugal force begins to dominate the buoyancy force.

For straight tubes, we compare in figure 7 the numerical computations of the ratio of average heat transfer rates with Morton's perturbation result (1959)

$$Q_b/Q_s = 1-0{\cdot}2100(ReRa/4608)^2+\dots .$$

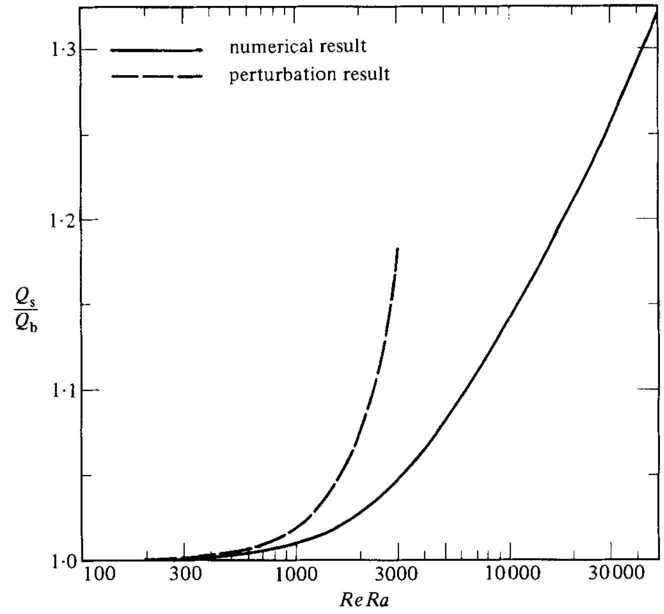

FIGURE 7. Variation of the average heat-transfer ratio Q_s/Q_b with *ReRa* in straight tubes.

Here Q_b is the average rate of heat transfer for flow through a straight tube with buoyancy, for a given pressure gradient. Again, Morton's result overpredicts Q_s/Q_b by

(i) 1 % at $ReRa = 2000$,
(ii) 5 % at $ReRa = 3000$,
(iii) 11 % at $ReRa = 4000$.

For $ReRa > 4000$, the missing higher-order terms cause the perturbation result to diverge rapidly from the numerical result. Note the decrease in Q_b/Q_s with *ReRa*, due to the decrease in volume flux.

The perturbation solution by Yao & Berger (1978) predicts that $Q_s/Q_b = 1$. Consequently, the present numerical results extend well beyond the range of validity of the perturbation solution for global heat-transfer rates.

5.3 *Dimensionless stream function*

A third global variation, one which vividly portrays the interaction of the centrifugal and buoyancy forces, is brought out in a plot of lines of constant stream function f.

In figure 8 (*a*), lines of constant stream function are plotted for the case $ReRa = 0$, $De = 660$. In this case, only the centrifugal force is present and its action is to force the central core towards the outer bend. This results in a stagnation-point flow at $\psi = 90°$, with fluid moving away along the wall. Two vortices, opposite in sign and equal in magnitude, occur with a dividing streamline being the diameter through $\psi = 90°$.

In figure 8 (*b*), lines of constant stream function for the case $ReRa = 5000$, $De = 0$ are plotted. Only the buoyancy force is present in this case. Our thermal boundary condition is that of a constant axial temperature gradient. Furthermore, the rate of heat transfer from the wall to the core is finite. As a result, fluid in the core is cooler

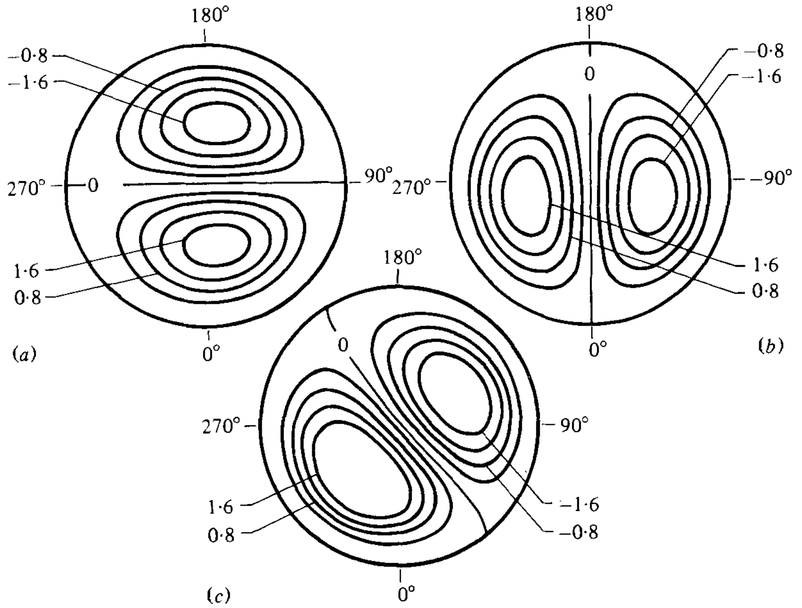

FIGURE 8. Lines of constant stream function: (*a*) $ReRa = 0$, $De = 660$; (*b*) $ReRa = 5000$, $De = 0$; (*c*) $ReRa = 5000$, $De = 660$.

and denser than fluid near the walls. Under the influence of a gravitational field, the central core falls towards the bottom of the tube at $\psi = 0°$. A stagnation-point flow is developed there with fluid moving away along the walls, getting hotter as it moves up along the walls. Again, two vortices, opposite in sign and equal in magnitude, are developed with a dividing streamline being the diameter through $\psi = 0°$.

When both centrifugal and buoyancy forces are important, the result is to turn the dividing streamline to an angle intermediate between $\psi = 0°$ and $\psi = 90°$. Also, the dividing streamline is, in general, a curved line through the centre. This effect is demonstrated in figure 8(*c*), where lines of constant stream function for the case $ReRa = 5000$, $De = 660$ are plotted.

5.4 *Local effects*

It is known that stagnation-point flows increase the local heat-transfer rates. Points of separation have an opposite effect. Since buoyancy effects help to determine the positions of the stagnation and separation points along the wall, buoyancy must be a factor in the local variation of heat-transfer rates. Our computations have revealed that this is indeed the case.

In addition, the local variation of axial shear stress τ_{rz} and circumferential shear stress $\tau_{r\psi}$ depend upon $ReRa$ as well as De. These shear stresses are calculated in our numerical solutions according to

$$\tau_{rz} = \left(\frac{\partial w}{\partial r}\right)_{r=1}, \quad \tau_{r\psi} = \left(\frac{\partial^2 f}{\partial r^2}\right)_{r=1}. \tag{19}$$

The point of maximum axial shear stress tends to follow the stagnation point closely. This is because the maximum axial velocity always tends to be along the dividing streamline. The point of maximum circumferential shear stress is generally

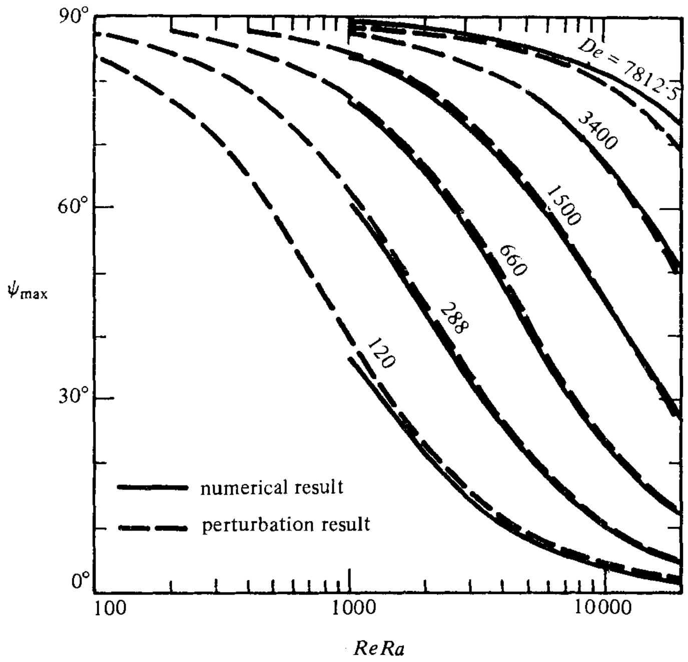

FIGURE 9. Position of maximum heat transfer.

located 90° or less away from the stagnation points, for this is where the secondary velocity v assumes its greatest magnitude.

The numerical computations of the points of maximum heat transfer and axial shear stress are compared directly with the perturbation results of Yao & Berger (1978). The maximum points are interpolated from the numerical data and should be accurate to $\pm 2°$.

Positions (denoted by $\psi_{\max}$) of maximum heat transfer and axial shear stress are compared in figures 9 and 10 respectively. Here the curves represent lines of constant De. The most striking observation is that the numerical results, for the most part, do not differ appreciably from the perturbation results given in Yao & Berger (1978) as

$$\psi_{\max} = \arctan \frac{(3+8{\cdot}05\,Pr)}{(1+2{\cdot}16\,Pr)} \frac{2De}{ReRa}$$

for positions of maximum heat transfer

$$\psi_{\max} = \arctan \frac{6De}{ReRa}$$

for positions of maximum axial shear stress. This is due to the fact that $\psi_{\max}$ depends only upon the ratio of De to $ReRa$ and not upon the absolute magnitudes of these parameters. It appears that the perturbation result is capable of giving quantitatively good values for $\psi_{\max}$ over a large part of the $ReRa$ and De range covered by the numerical computations. Only for the larger values of $ReRa$ and intermediate values of De does $\psi_{\max}$, as predicted by the perturbation solution, diverge noticeably from the numerical results. One further observes from the figures that all curves begin near $\psi_{\max} = 90°$. In this region $ReRa$ is small. As a result, the centrifugal force dominates the buoyancy force and $\psi_{\max}$ is little different from the value $\psi_{\max} = 90°$ that occurs

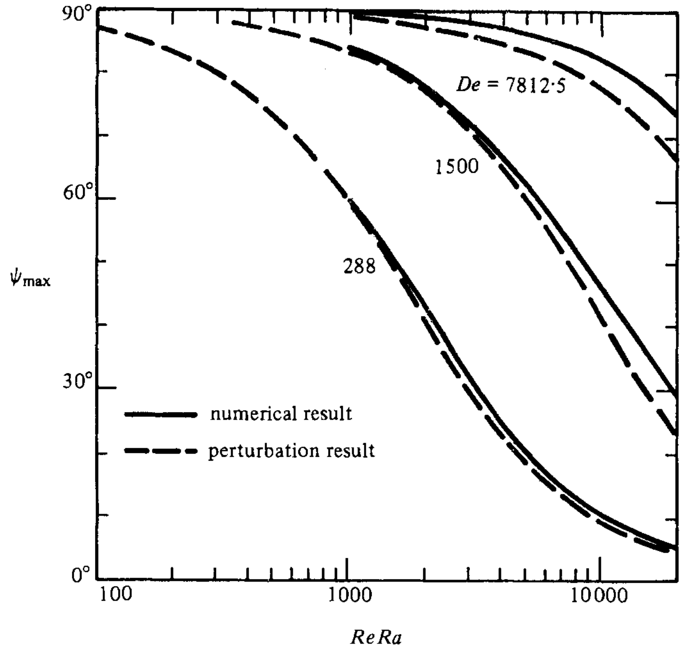

FIGURE 10. Position of maximal axial shear stress.

for curved tube flows without buoyancy ($ReRa = 0$). At this limiting case, the numerical and perturbation results match exactly. Since we anticipated that the perturbation solution would match closely the numerical results for smaller values of *ReRa*, the first non-zero value of *ReRa* calculated was $ReRa = 1000$. As the strength of the buoyancy force increases, the dividing streamline rotates towards $\psi = 0°$. This causes ψ_{max} to decrease towards 0°. Eventually, the centrifugal force is dominated by the buoyancy force, and ψ_{max} is little different from the value $\psi_{max} = 0°$ that occurs for flow through straight tubes where there is no centrifugal force. As *De* increases, the curves are seen to remain near 90° for a larger distance before dropping towards 0°. The reason is simply that the buoyancy force has to match and overcome a more powerful centrifugal force before it can significantly alter the flow and heat-transfer rates.

The numerical values for positions of maximum circumferential shear stress are shown in figure 11 in the form of curves of constant *De*. One observes that all curves, with the exception of $De = 0$, begin somewhat above 0°, with the distance above 0° increasing with *De*. These initial points represent flows without buoyancy force present. As *De* increases, the vortex centres, or points of maximum circulation, are pushed by the centrifugal force towards the outer bend of the tube. This results in movement of the points of maximum circumferential shear stress towards the outer bend, or from $\psi = 0°$ towards $\psi = 90°$.

The entire curve $De = 0$ represents flow without centrifugal force. Here the maximum point is observed to increase from $\psi = 270°$ as the buoyancy force increases. The increasing buoyancy force pushes the vortex centres towards the bottom of the tube. As a result, ψ_{max} increases from $\psi = 270°$ towards $\psi = 0°$ as *ReRa* increases.

With increasing *ReRa*, the curves of constant non-zero *De* decrease towards the

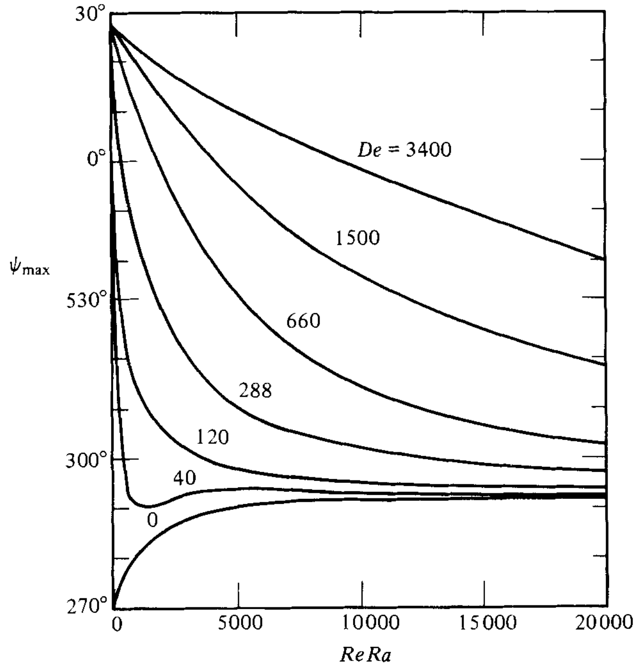

FIGURE 11. Position of maximum circumferential shear stress.

curve $De = 0$. Thus the pure buoyancy case acts as a limiting case, which the other curves approach asymptotically as $ReRa \rightarrow \infty$. This is simply due to the continued growth of the buoyancy force. First, the centrifugal force dominates the buoyancy force, and the curve remains far above the pure buoyancy curve. As the buoyancy force grows, the curve drops. Finally, as the buoyancy force begins to dominate the centrifugal force, the curve flattens out and slowly approaches the curve for $De = 0$.

The curve $De = 40$ represents an interesting case. Since the centrifugal force is very small, it quickly becomes dominated by the increasing buoyancy force. As a result, the curve drops so steeply that it approaches the pure buoyancy case before that curve has finished its initial period of rapid rise. Thus the $De = 40$ curve first decreases and then gradually increases in conjunction with the $De = 0$ curve.

5.5. *Regional Map*

In figure 12, we consider the $(ReRa, \kappa)$-plane, which is seen to be separated into three distinct regions. The first region *I* is where the centrifugal force dominates. Here the momentum and energy equations may be treated as though they are uncoupled. In the second region *II* both buoyancy and centrifugal forces are important. As a result, problems that fall into this region need to be dealt with by using the general equations (4). The third region *III* represents a simplification of the heated-curved-tube problem. Here buoyancy force dominates the centrifugal force. Thus problems which lie in this region may be treated as though a straight tube with buoyancy forces were being investigated.

Our criterion for establishing the boundaries of these regions is a 5 % variation in the value of the average heat-transfer rate Q from the values to be expected for flow with only centrifugal force or flow with only buoyancy force.

Note that the regional map essentially summarizes the major point of this paper;

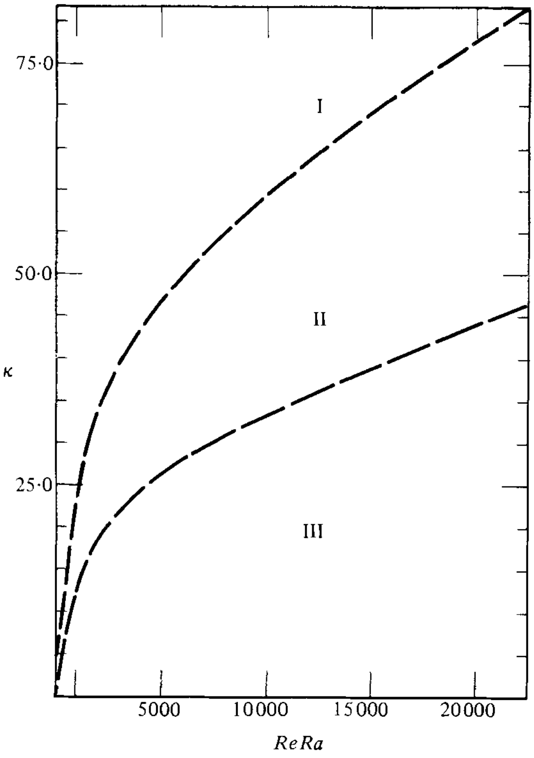

FIGURE 12. Regimes of flow.

that is, buoyancy affects both global and local variables characterizing flow through heated curved tubes. However, the centrifugal and buoyancy forces are not always of the same order of magnitude. When the buoyancy force is weak, it may be dominated by the centrifugal force, and vice versa.

REFERENCES

AKIYAMA, M. & CHENG, K. C. 1971 Boundary vorticity method for laminar for forced convection heat transfer in curved pipes. *Int. J. Heat Mass Transfer* **14**, 1659–1675.

BARUA, S. N. 1963 On secondary flow in stationary curved pipes. *Q. J. Mech. Appl. Math.* **16**, 61–77.

COLLINS, W. M. & DENNIS, S. C. R. 1975 The steady motion of a viscous fluid in a curved tube. *Q. J. Mech. Appl. Math.* **28**, 133–156.

DEAN, W. R. 1928 The streamline motion of fluid in a curve pipe. *Phil. Mag.* **5**, 673–695.

DENNIS, S. C. R. 1980 Calculation of the steady flow through a curved tube using a new finite-difference method. *J. Fluid Mech.* **99**, 449–467.

FOX, L. 1947 Some improvements in the use of relaxation methods for the solution of ordinary and partial differential equations. *Proc. R. Soc. Lond.* A **190**, 31–59.

ITO, H. 1969 Laminar flow in curved pipes. *Z. angew. Math. Mech.* **49**, 653–663.

KALB, C. E. & SEADER, J. D. 1972 Heat and mass transfer phenomenon for viscous flow in curved circular tubes. *Int. J. Heat Mass Transfer* **15**, 801–817.

MCCONALOGUE, D. J. & SRIVASTAVA, R. S. 1968 Motion of a fluid in a curved tube. *Proc. R. Soc. Lond.* A **307**, 37–53.

Mori, Y. & Nakayama, W. 1965 Study on forced convective heat transfer in curved pipes (1st report, laminar region). *Int. J. Heat Mass Transfer* **8**, 67–82.

Morton, B. R. 1959 Laminar convection in uniformly heated horizontal pipes at low Rayleigh numbers. *Q. J. Mech. Appl. Math.* **12**, 410–420.

Ozisik, M. N. & Topakoglu, H. C. 1968 Heat transfer for laminar flow in a curved pipe. *Trans. A.S.M.E.* C: *J. Heat Transfer* **90**, 313–318.

Patankar, S. V., Pratap, V. S. & Spalding, D. B. 1974 Prediction of laminar flow and heat transfer in helically coiled pipes. *J. Fluid Mech.* **62**, 539–551.

Rabadi, N. J., Chow, J. C. F. & Simon, H. A. 1979 An efficient numerical procedure for the solution of laminar flow and heat transfer in coiled tubes. *Numer. Heat Transfer* **2**, 279–289.

Seban, R. A. & McLaughlin, E. F. 1963 Heat transfer in tube coils with laminar and turbulent flow. *Int. J. Heat Mass Transfer* **6**, 387–395.

Simon, H. A., Chang, M. H. & Chow, J. C. F. 1977 Heat transfer in curved pipes with pulsatile, fully developed laminar flows. *Trans A.S.M.E.* C: *J. Heat Transfer* **99**, 590–595.

Southwell, R. V. 1946 *Relaxation Methods in Theoretical Physics*. Oxford University Press.

Taylor, G. I. 1929 The criterion for turbulence in curved pipes. *Proc. R. Soc., Lond.* A **124**, 243–249.

Van Dyke, M. 1978 Extended Stokes series: laminar flow through a loosely coiled pipe. *J. Fluid Mech.* **86**, 129–145.

Yao, L. S. & Berger, S. A. 1978 Flow in heated curved pipes. *J. Fluid Mech.* **88**, 339–354.

Yee, G. & Humphrey, J. A. C. 1979 Developing laminar flow and heat transfer in strongly curved ducts of rectangular cross-section. *A.S.M.E. Paper* no. 79-WA/HT-15.

Zapryanov, Z., Christov, C. H. & Toshov, E. 1980 Fully developed laminar flow and heat transfer in curved tubes. *Int. J. Heat Mass Transfer* **23**, 873–880.